Failure behavior of 70/30 brass lattice structure with a proposed cell topology produced by rapid investment casting

Arya Aditya Nugraha[1*] and *Akhmad* Ardian Korda[1]

[1]Department of Metallurgical Engineering, Faculty of Mining and Petroleum Engineering, Institut Teknologi Bandung, Jl. Ganesha, 10, Bandung, 40132, Jawa Barat, Indonesia

Abstract. Lattice structures are unique architectural configurations with repeated unit cells and significant void spaces, offering exceptional specific strength, stiffness, and energy absorption capacity. These properties make them ideal for lightweight structures and mechanical dampers. Rapid investment casting, a blend of investment casting and 3D printing, emerges as a promising method for metal lattice structure production. It outperforms typical metal additive manufacturing, yielding products with fewer defects. A proposed cell topology has been introduced, striking an optimal balance between printability, castability, tensile strength, and shear strength. To explore its performance under compressive loading, 70/30 brass lattice structures with two varying heights were fabricated using rapid investment casting and evaluated. Shorter samples displayed uniform expansion within each cell row, while taller ones experienced abrupt shear fractures, resulting in lower absorbed energy. Detailed microstructure observations and additional mechanical properties were obtained, enhancing the understanding of failure behavior. In conclusion, rapid investment casting combined with the proposed cell topology opens exciting possibilities for manufacturing high-performance lattice structures with improved mechanical characteristics.

1 Introduction

Lattice structures have the ability to decrease the material used, leading to a reduction in component weight, while still providing adequate strength [1], [2]. Metal lattice structures, also referred to as cellular metals, exhibit similar properties by combining the properties of cellular materials with those of metals. Metals typically possess high strength and toughness, while cellular materials are characterized by their high energy absorption capacity, low density, and easy fluid flow access [3]. As a result, these structures have unique mechanical properties, particularly with regard to high stiffness and heat transfer control [4], [5]. In some other references, metal lattice structures are also referred to as porous metals, as they possess a relatively larger volume fraction of voids or pores compared to their solid fraction compared to metal forms in general [6].

Metal lattice structures have been attracting attention in various fields due to their numerous advantages, particularly in relation to lightweight structures. One example of this is in the biomedical field, where metal lattices are used for creating lightweight bone scaffolds that serve as temporary mechanical supports. Through topology modifications of a lattice structure, various properties can be improved with ease. Consequently, orthopedic implant designs can be optimized for the specific installation location, which can promote bone growth [7]. Additionally, metal lattice applications have also been applied to aerospace technology [8]–[10], mechanical dampening structures, structures experiencing heat exchange between fluids and solids, electrodes, and catalysts [11].

Rapid investment casting is a manufacturing method capable of producing a metal lattice [12]. This method combines investment casting with 3D printing (3DP) technology, specifically for the pattern making stage [13], [14]. Typically, the patterns for 3D printing are made from a group of polymer materials. There are several types of 3D printing methods, but stereolithography (SLA) is particularly interesting due to its high dimensional accuracy and smooth surface quality [15], [16]. A well-designed lattice topology can directly support existing complex overhangs, which is generally beneficial as it can enhance the manufacturability of a series of lattice structure manufacturing processes [17]. Moreover, rapid investment casting shows potential as a more attractive option than metal 3D printing for manufacturing metal lattices, considering the limitations of metal 3D printing. Rapid investment casting produces defects such as porosity, internal cracking, evaporation of certain elements like magnesium and zinc, and distortion due to residual stresses that are not as high as those typically produced by metal 3D printing [18]–[20]. In addition, the cost of rapid investment casting can be reduced, for

* Corresponding author: arya.magister@gmail.com

example, one of the approaches is to print patterns using low-cost plastic materials [21].

A lattice structure is defined based on the topology of its constituent unit cells. Topology refers to the pattern of strut and void distribution within a unit cell. It is one of the most significant factors affecting various lattice performance aspects, such as manufacturability and mechanical properties [21]–[24]. Poor manufacturability can lead to the emergence of defects during the manufacturing process, which in turn can adversely affect the mechanical properties of the lattice being produced. Therefore, numerous studies have been conducted to investigate the properties exhibited by various topologies [25]–[28].

The proposed cell topology published by Christopher T. Richard and Tsz Ho Kwok in 2021 is a newly developed lattice topology that has grabbed the authors' interest. Its design is particularly focused on ensuring that it can be manufactured effectively using rapid investment casting. Furthermore, according to the Finite Element Analysis (FEA) results, this topology still exhibits superior mechanical properties, including tensile and shear strength, compared to several other widely used topologies. This topology shows an optimal combination of printability, castability, tensile, and shear strength [29].

The proposed cell represents an open-cell structure, where all voids are interconnected [30]. In contrast, materials like aluminum foam consist mainly of closed-cell structures, where each void is not interconnected [31], [32]. The proposed cell is assembled by stacking cubes to form a lattice structure. This topology features straight struts with circular cross-sections.

Research on the mentioned topology has been limited thus far, and there is currently no available data on direct mechanical testing of the metal lattices produced. To address this gap and build upon previous studies, this research focuses on the metal lattice structures with a proposed cell topology produced by rapid investment casting. A series of experiments were conducted to explore the fracture and failure behavior of the lattice. Specifically, samples were made of 70/30 brass in two variations of height and then subjected to a compression test. Microstructure was observed then the mechanical properties were also calculated and analyzed.

2 Material and Methods

2.1 Sample design

Lattice structures with different numbers of unit cells were developed using Autodesk Inventor Professional 2022. The first structure has dimensions of 2×2×8 unit cells, while the second one consists of 2×2×4 unit cells. Each structure has the same strut diameter, lattice parameter, and density, which are 2.222 mm, 10 mm, and 20%, respectively. Figure 2 provides a detailed view of both structures, with the blue arrow aligned along the Z-axis indicating the direction of metal filling during the subsequent casting process.

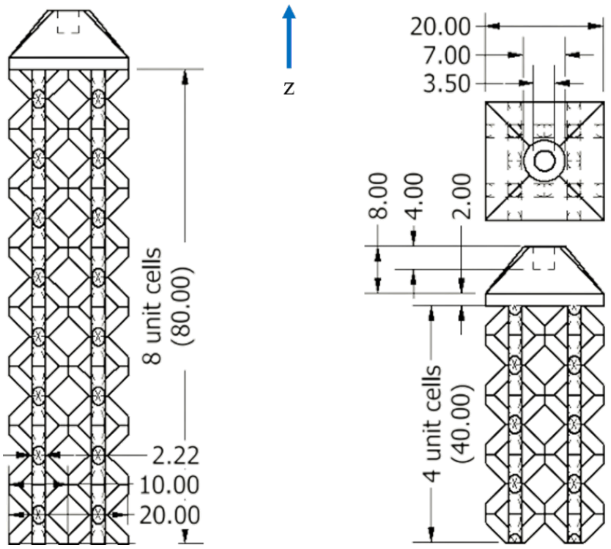

Fig. 1. The structures with a proposed cell topology on the left and right have heights of 4 and 8 unit cells, respectively, with their sizes in the image being proportionally related. The length units in the image are represented in millimeters.

2.2 Manufacturing Process

2.2.1. Pattern Making

The casting patterns were created using the Form 2 SLA 3D printer (Formlabs, United States) with BlueCast Original for Formlabs castable resin (BlueCast, Italy) as the material. The 3DP process had a 100 μm resolution in the Z direction.

2.2.2. Molding

The patterns were soldered with wax to resemble a tree. The wax tree was placed on the black rubber mold base, as shown in Fig. 2(a). The wax used is Jade Green SCP Wax (Siam Casting Powder, Thailand). Then, a steel flask that had been completely insulated was also attached to the rubber base. The flask has an outer diameter of 9 mm and has holes measuring 1 cm in diameter.

The mold material comprises a slurry created by blending investment powder with reverse osmosis (RO) water. The selected investment powder is RESINCAST (Chang Jewelry Powder, Thailand). The molding process, from mixing both raw materials to pouring the slurry into the flask, was carried out using the St. Louis 2000-14 PT vacuum mixing machine (CIMO, Italy). After the slurry hardened, the flask was then subjected to a burnout process using a BU 440T Burnout Furnace (Old Moon, Thailand). The overall molding process adheres to the procedure provided by the powder manufacturer.

2.2.3. Casting

The alloy used is 926 Yellow Brass (ABI, Thailand), and its chemical compositions are listed in Table 1. When the burnout stage was almost complete, the alloy was placed into a crucible that had been preheated in a vacuum casting machine of Indutherm VC 450 (Indutherm, Germany). The machine brought the feed temperature to 1080 °C. The molten metal was then held at this temperature for about 40 seconds before finally being lowered to the pouring temperature of 1040 °C. The mold that had been filled with the alloy was removed from the machine, followed by air-cooling for approximately 25 minutes until its temperature at least reached 250°C.

Table 1. Chemical compositions of 926 yellow brass (wt %) tested using GOLDSCOPE SD 520 XRF (Fischer, Germany).

(%)						
Cu	**Zn**	**Au**	**Bi**	**Pb**	**Ag**	**Fe**
73.20	26.54	0.13	0.04	0.04	0.04	0.01

2.2.4. Quenching and Post Processing

The cooled flask was quenched in room temperature water. The metal tree inside was sprayed with pressurized water to remove any remaining mold material. Once the attached mold material had been completely removed, the metal tree was fed into an Electromagnetic-Polishing Machine EPM4-30 (Old Moon, Thailand), leaving a shiny metal tree without any remaining debris on its surface. In this machine, the metal tree was placed inside a cylinder filled with water mixed with a polishing compound and containing stainless steel needles that rotate electromagnetically. The castings that had been cut from the metal trees are shown in Fig. 2(b,c). This step is considered not to affect the geometric accuracy of the resulting metal tree.

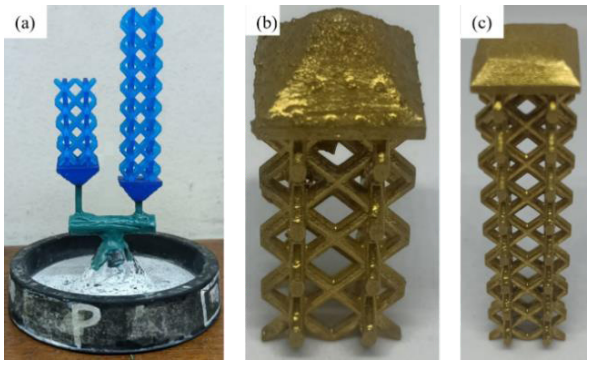

Fig. 2. The wax tree that is placed on the base with the patterns of 4 unit cell heights on the left and 8 unit cell heights on the right (a). The castings of 4 (b) and 8 (c) unit cell heights that have been polished and cut from the metal tree.

2.3 Experiment setup

2.3.1. Compression test

The compression test samples consist of brass lattice structures with two different heights: 2 unit cells and 6 unit cells. These samples were obtained by removing the top and bottom rows of each casting. Figure 3 shows the schematic illustration of the compression test samples obtained from the brass lattice structure. Compression tests were carried out using a Hung Ta Universal Testing Machine with a constant compressive strain rate of 1 mm/minute. The deformation behavior during the compression was also recorded at 30 frames per second (fps).

2.3.2. Characterization

Microstructure characterization using optical microscopy (OM) and scanning electron microscopy (SEM, JEOL6510) was performed on the cross-sectional view of a 6-strut branch, as depicted in Fig. 3. The sample preparation involved several sequential stages, including mounting, grinding, polishing, and etching. Grinding was performed using sandpaper with progressively finer grit sizes, ranging from 180 to 2000. Polishing was carried out using a polishing cloth and alumina paste. Etching was conducted by immersing the samples in a solution consisting of 5 mL of HNO_3 dissolved in 5 mL of distilled water for 10-15 seconds. For SEM observation, a carbon coating was applied initially.

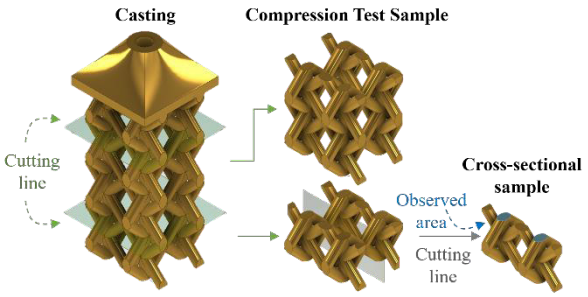

Fig. 3. Schematic illustration of obtaining the compression test sample and cross-sectional sample.

3 Results and Discussion

3.1 Microstructure

Microstructure characterization was conducted to observe the dendritic structure in the as-cast samples. Figure 4 shows OM microstructure images of a cross-section of a 6-strut branch sample, depicting the dendritic structures as indicated within the blue dashed line rectangular shape. Distinct differences in etching colors are noticeable among the dendrites in various regions. Similar differences have been previously illustrated, and their correlation with grain orientation has been detailed in the work conducted by Szabo et al [33]. This observation further strengthens the presence of dendrite growth in those directions. In addition, the investigation shows no macroscopic defect is also detected from the as-cast sample.

Figure 5 illustrates the presence of dendrites in an area with different colors. The dendrites appear to have

different growth directions, from the outer to the inner. The growth direction of dendrites is opposite to the heat release direction. In other words, dendrites grow in the same direction as the solidification or freezing direction. A cluster of dendrites with the same growth direction will form a grain [34]. The appearance of dendrites is also observed using SEM, as shown in Fig. 6.

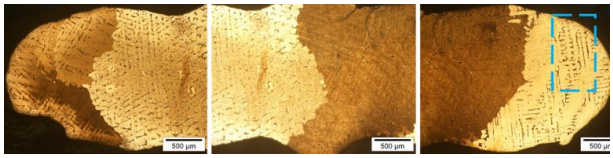

Fig. 4. The OM microstructure images of a cross-section of a 6-strut branch sample with a 20x magnification depicted the dendritic structures as indicated within the blue dashed line rectangular shape.

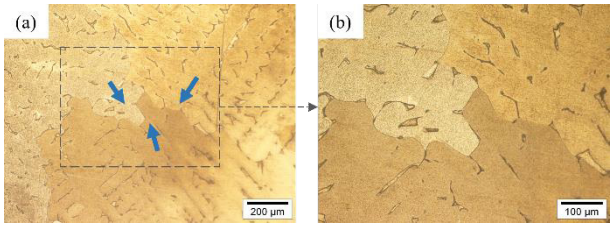

Fig. 5. Dendrite growth in different directions observed using OM with a magnification of 50x (a) and 100x (b). Blue arrows indicate the direction of dendrite growth.

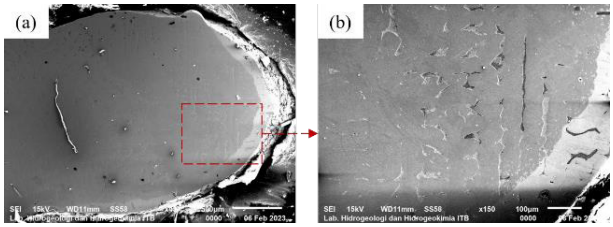

Fig. 6. The SEM observation result (a). The appearance of dendrites in the red area (b).

3.2 Mechanical Properties

The compression tests were conducted to provide some mechanical properties data for the 70/30 brass lattice structure with the proposed cell topology produced by rapid investment casting that has not been directly tested before. The results of the tests are also expected to validate the predicted compressive strength derived from finite element analysis (FEA) in Richard and Kwok's work [29]. This test was feasible because all the castings were fully filled. Removal of the top and bottom rows to obtain the specimens was done because these areas tend to be the locations of defects [23]. The brass used in this research was chosen due to its composition ratio of Cu and Zn, which closely approximates the 70:30 ratio. This choice aims to closely match the material demonstrated by Richard and Kwok's work. The cell density is also designed to be 20% for the same reason. In addition to its relatively low cost, brass is also used because it is easy to cast.

The compression test curves of samples with heights of 2 and 6 unit cells are depicted in Fig. 7. The test was conducted twice for each sample variation, and then one of the better curves was selected. A summary of the mechanical properties data processed from the curves is presented in Table 2. Young's modulus (E) is the slope of the regression result in the linear region. Yield strength (σ_y) is obtained from the intersection of the curve with a line parallel to the regression result in the linear region that intersects the X-axis at 0.2% strain [35]. Plateau stress (σ_{pl}) is calculated as the average stress value between 20-60% strain. The plateau phase ends when the stress reaches 1.3 times the plateau stress and then continues to increase. Densification strain (ε_d) is the strain value when the plateau phase ends. Absorbed energy (AE) is the area under the curve from zero strain to densification strain [23]. The effective cross-sectional area is used to calculate stress values related to the aforementioned variables. The effective cross-sectional area is the average of the largest and smallest sample cross-sectional areas [32].

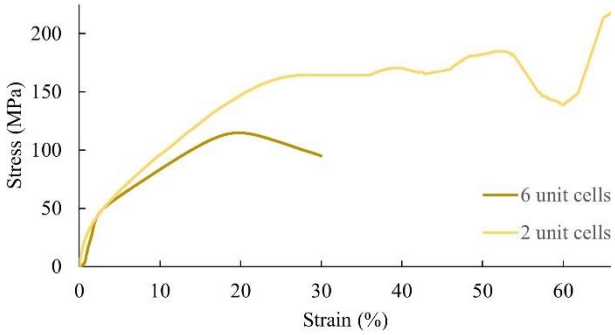

Fig. 7. The stress-strain curves for each compression test sample.

The sample with the height of 2 unit cells, or the shorter sample, lasted until the densification phase. Its curve demonstrated a gradual increase even after surpassing its yield strength, a phenomenon also observed in the study by Costanza et al [32]. The decrease in the curve during the plateau phase indicates significant deformation in the structure or even fractures of the struts. The curve can increase again in this phase when the deformed parts overlap with the parts that have not been deformed yet [24]. The curve is still acceptable when compared to some of these other studies that have also experienced similar patterns. In contrast, the sample with the height of 6 unit cells, or the taller one, did not exhibit a plateau and densification phase. The taller sample experienced abrupt shear failure and detachment, leading to test termination shortly after stress exceeded the yield strength.

Table 2. The mechanical properties of the 70/30 brass lattice structure with the proposed cell topology and the density of 20%.

Quantities	Units	Values
Young's modulus (E)	GPa	1.1
Yield strength (σ_y)	MPa	75.1
Plateau stress (σ_{pl})	MPa	165
Densification strain (ε_d)	%	65
Absorbed energy (AE)	J/cm^3	93

Table 2 only processed data from the shorter sample curve. This sample is considered to represent the mechanical properties of the 70/30 brass lattice structure

with the proposed cell topology and the density of 20%. This choice is based on the more comprehensive data available from this sample. Young's modulus reflects a material's stiffness, which is often inversely related to its energy absorption capacity. Low energy absorption capacity tends to cause objects to crack rather than deform first when subjected to stress [36].

Table 3. The prediction of the range of mechanical properties values of the compression test samples.

Quantities	Units	Scaling Laws	Values
Young's modulus (E)	GPa	$(0,1\text{-}4)\ E_s\ \rho^2$	0.44-17.60
Yield strength (σ_y)	MPa	$(0,1\text{-}1)\ \sigma_{y,s}\ \rho 1,5$	0.84-8.50
Plateau stress (σ_{pl})	MPa	$(0,25\text{-}0,35)\ \sigma_{y,s}\ \rho 1,6$	1.80-2.54
Densification strain (ε_d)	%	$(90\text{-}100)(1 - 1,4\rho + 0,4\ \rho^3)$	65.08-72.32
Absorbed energy (AE)	J/cm^3	$\sigma_{pl}\ \varepsilon_d$	1.17-1.83

The taller sample experienced less strain compared to the shorter sample. However, the taller sample has already shown lower absorbed energy for the same strain. This decrease in absorbed energy is directly proportional to the height-to-width ratio of the samples. The sample with the height of 2 unit cells has the ratio of 1, while the sample with the height of 6 unit cells has the ratio of 3. A higher ratio tends to cause deformation to occur in an unstable manner. One of the indications of this instability is the significant drop in stress value after it passes the yield strength [24].

Table 3 shows the prediction of the range of mechanical properties values of the compression test samples based on Gibson and Ashby scaling laws. The 's' code for the variables in the table refers to the condition when the material is in a solid form. The mechanical properties data used for the solid state of the 70/30 brass were typically similar to the material data for cartridge brass, with E_s 266 of 110 GPa and σ_y of 95 MPa. Cartridge brass is a common choice for the majority of bullets, especially for the cartridge case, and its composition is similar to that of 70/30 brass [37].

It can be seen that the Young's modulus value in this experiment is within the predicted range. The densification strain value is only slightly below the prediction. The conformity of the prediction in these two parameters can be used as a basis to say that the test and data processing performed are accurate enough. The other three parameters are far above the prediction. Only the values of Young's modulus and yield strength are within the predicted range. Gallien [23] stated that the discrepancy in predicted values for the other three parameters is reasonable since scaling laws were originally intended for stochastic cellular metals [31]. However, at least scaling laws can still be used to provide an initial estimate of the mechanical properties values of a metal lattice structure. In addition, the values that are higher than the prediction are advantageous. This shows that the yield strength, plateau stress, and absorbed energy of the lattice structures in this study are much higher than most stochastic cellular metals made from the same material and density.

Furthermore, the Young's modulus value of the brass 70/30 from this experiment is significantly higher than the value predicted by Richard and Kwok through FEA, which is only 23.6 MPa. The value predicted by Richard and Kwok is also inconsistent with predictions made using scaling laws.

3.3 Deformation Behavior

Recordings during compression tests were carried out to observe the deformation behavior of the samples. Several deformation phenomena of both compression test samples at certain strains are depicted in Fig. 8. Figure 8 also helps visualize the results in Fig. 7 and Table 2. The phenomena in Fig. 8 include samples in the initial state, the linear deformation limit, when a crack or a certain form of deformation first appears, and when densification or a final fracture occurs.

Both samples experience linear deformation up to a strain of about 6%. Then both samples experience plastic deformation as strain increases. At this stage, the sample with the height of 2 unit cells appears to expand evenly in each row. Li et al.'s testing also showed uniform deformation until the sample resembled a barrel shape [22]. Finally, both samples experienced densification, which started at approximately 65% strain. Both samples did not show any visible cracks during the test.

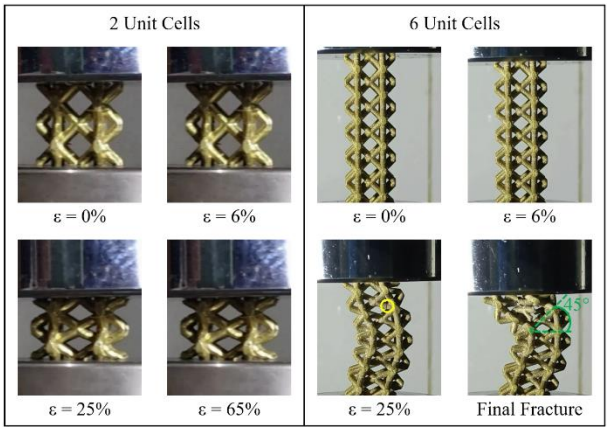

Fig. 8. The deformation behavior of compression test samples with the height of: (a) 4; (b) 6 unit cells. The yellow circle indicates the crack near the middle branching area. The green line indicates the shearing direction.

The sample with the height of 6 unit cells still has approximately the same linear limit as the shorter one. When plastic deformation occurs, at a strain of approximately 25%, the taller sample shows a crack initiated only near the middle branching area. This sample shows buckling, which is not observed in the shorter sample. Finally, the taller sample experiences a sudden diagonal shear fracture at a 45° angle to the loading

direction, resulting in the termination of the test upon sample release. This direction is in line with the maximum shear stress orientation on a stress plane. The cracks and buckling increase the local stress concentration around them, thereby triggering simultaneous cracks in branches that are in a 45° shear band [22]. The shear band is an area where shear stress is concentrated.

The phenomenon of changes in deformation behavior between samples with different heights or height-to-width ratios is in accordance with the results of Zhao et al.'s research. Lower-ratio samples tend to exhibit row-by-row deformation or uniform deformation. As the ratio increases, this deformation behavior transitions into a sudden diagonal shear fracture. This phenomenon corresponds to the explanation provided in the preceding subsection, which addresses the issue of unstable deformation in samples with higher ratios. The occurrence of sudden diagonal shear fractures must be avoided when using such structures for mechanical damping purposes. In the previous subsection, Fig. 7 and Table 2 have demonstrated that a metal lattice, especially one made of brass, possesses a relatively high energy absorption capacity, a critical requirement for a mechanical damper structure. However, the size of the metal lattice still needs to be optimized to ensure the safe dissipation of externally applied impact energy through deformation, crushing, or fracture behavior, without significantly reducing the amount of energy absorbed [24].

4 Conclusion

Based on the results and discussion of compression tests carried out on 70/30 brass lattice structures with a proposed cell topology and a density of 20%, produced by rapid investment casting, the following conclusions can be derived:

1. The absorbed energy of the samples reaches 93 J/cm^3.
2. The deformation behavior of the lattice structures is influenced by their height-to-width ratio. Shorter samples with a ratio of 1 exhibit uniform deformation within each cell row. In contrast, taller samples with a ratio of 3 experience shear fracture at a 45° angle relative to the loading direction. Samples with higher ratios also demonstrate lower absorbed energy.
3. The Young's modulus and yield strength of the samples are 1.1 GPa and 75.1 MPa, respectively.

Acknowledgment

This research did not receive any specific grant from funding agencies in the public, commercial, or not-for-profit sectors.

References

1. G. Dong, Y. Tang, D. Li, and Y. F. Zhao, ‘Design and optimization of solid lattice hybrid structures fabricated by additive manufacturing’, *Addit Manuf*, **33** (2020)
2. L. Xiao, X. Xu, G. Feng, S. Li, W. Song, and Z. Jiang, ‘Compressive performance and energy absorption of additively manufactured metallic hybrid lattice structures’, *Int J Mech Sci*, **219** (2022)
3. R. Goodall and A. Mortensen, ‘Porous Metals’, in *Physical Metallurgy: Fifth Edition*, 2399–2595 (2014)
4. S. Y. Choy, C. N. Sun, K. F. Leong, and J. Wei, ‘Compressive properties of Ti-6Al-4V lattice structures fabricated by selective laser melting: Design, orientation and density’, *Addit Manuf*, **16**, 213–224 (2017)
5. T. Maconachie *et al.*, ‘SLM lattice structures: Properties, performance, applications and challenges’, *Materials and Design*, **183** (2019)
6. A. Nouri and P. D. Hodgson, ‘Biomimetic Porous Titanium Scaffolds for Orthopedic and Dental Applications 415 X Biomimetic Porous Titanium Scaffolds for Orthopedic and Dental Applications’ (2010)
7. L. Yan, L. P. Zhao, and G. K. O’neill, ‘Dimensional consistency of SLM printed orthopaedic implants designed using lightweight structures’ (2020)
8. X. Geng, L. Ma, C. Liu, C. Zhao, and Z. F. Yue, ‘A FEM study on mechanical behavior of cellular lattice materials based on combined elements’, *Materials Science and Engineering A*, **712**, 188–198 (2018)
9. M. Kaur, T. G. Yun, S. M. Han, E. L. Thomas, and W. S. Kim, ‘3D printed stretching-dominated micro-trusses’, *Mater Des*, **134**, 272–280 (2017)
10. B. Lozanovski *et al.*, ‘Computational modelling of strut defects in SLM manufactured lattice structures’, *Mater Des*, **171** (2019)
11. J. Banhart, ‘Manufacture, characterisation and application of cellular metals and metal foams’, (2001)
12. Y. Huang, Y. Xue, X. Wang, and F. Han, ‘Effect of cross sectional shape of struts on the mechanical properties of aluminum based pyramidal lattice structures’, *Mater Lett*, **202**, 55–58 (2017)
13. N. Badanova, A. Perveen, and D. Talamona, ‘Study of SLA Printing Parameters Affecting the Dimensional Accuracy of the Pattern and Casting in Rapid Investment Casting’, *Journal of Manufacturing and Materials Processing*, **6**, 5 (2022)
14. C. K. Chua, C. Feng, C. W. Lee, and G. Q. Ang, ‘Rapid investment casting: Direct and indirect approaches via model maker II’, *International Journal of Advanced Manufacturing Technology*, **25**, 26–32 (2005)

15. M. Mukhtarkhanov, A. Perveen, and D. Talamona, 'Application of stereolithography based 3D printing technology in investment casting', *Micromachines*, **11** (2020)
16. N. Badanova, A. Perveen, and D. Talamona, 'Concise review on Pattern making process in Rapid Investment Casting: Technology, Materials & Numerical modelling aspect', *Advances in Materials and Processing Technologies*, **8**, 966–978 (2022)
17. X. Xue, C. Lin, F. Wu, Z. Li, and J. Liao, 'Lattice structures with negative Poisson's ratio: A review', *Materials Today Communications*, **34** (2023)
18. N. T. Aboulkhair, M. Simonelli, L. Parry, I. Ashcroft, C. Tuck, and R. Hague, '3D printing of Aluminium alloys: Additive Manufacturing of Aluminium alloys using selective laser melting', *Progress in Materials Science*, **106** (2019)
19. L. Zhang, J. Lifton, Z. Hu, R. Hong, and S. Feih, 'Influence of geometric defects on the compression behaviour of thin shell lattices fabricated by micro laser powder bed fusion', *Addit Manuf*, **58** (2022)
20. S. Wang *et al.*, 'Role of porosity defects in metal 3D printing: Formation mechanisms, impacts on properties and mitigation strategies', *Materials Today*, **59**, 133–160 (2022)
21. V. H. Carneiro, S. D. Rawson, H. Puga, J. Meireles, and P. J. Withers, 'Additive manufacturing assisted investment casting: A low-cost method to fabricate periodic metallic cellular lattices', *Addit Manuf*, **33** (2020)
22. P. Y. Li, Y. E. Ma, W. B. Sun, X. Qian, W. Zhang, and Z. H. Wang, 'Fracture and failure behavior of additive manufactured Ti6Al4V lattice structures under compressive load', *Eng Fract Mech*, **244** (2021)
23. F. Gallien, V. Gass, and A. Mortensen, 'Investment casting of periodic aluminum cellular structures using slurry-cast table salt moulds', *Mater Des*, **215** (2022)
24. P. Zhao, D. Huang, Y. Zhang, H. Zhang, and W. Chen, 'Microstructure and Properties of Hollow Octet Nickel Lattice Materials', *Materials*, **15** (2022)
25. S. E. Alkhatib, A. Karrech, and T. B. Sercombe, 'Isotropic energy absorption of topology optimized lattice structure', *Thin-Walled Structures*, **182** (2023)
26. J. Noronha *et al.*, 'Ti-6Al-4V hollow-strut lattice materials by laser powder bed fusion', *Addit Manuf*, **72** (2023)
27. D. Li, R. Qin, J. Xu, J. Zhou, and B. Chen, 'Topology optimization of thin-walled tubes filled with lattice structures', *Int J Mech Sci*, **227** (2022)
28. A. De Marzi, M. Vibrante, M. Bottin, and G. Franchin, 'Development of robot assisted hybrid additive manufacturing technology for the freeform fabrication of lattice structures', *Addit Manuf*, **66** (2023)
29. C. T. Richard and T. H. Kwok, 'Analysis and design of lattice structures for rapid-investment casting', *Materials*, **14** (2021)
30. M. Aramesh and B. Shabani, 'Metal foam-phase change material composites for thermal energy storage: A review of performance parameters', *Renewable and Sustainable Energy Reviews*, vol. **155** (2022)
31. M. F. Ashby, A. G. Evans, N. A. Fleck, L. J. Gibson, J. W. Hutchinson, and H. N. G. Wadley, 'Metal Foams: A Design Guide Library of Congress Cataloguing-in-Publication Data' (2000)
32. G. Costanza, A. Del Ferraro, and M. E. Tata, 'Experimental Set-Up of the Production Process and Mechanical Characterization of Metal Foams Manufactured by Lost-PLA Technique with Different Cell Morphology', *Metals (Basel)*, **12** (2022)
33. P. J. Szabo and I. Kardos, 'Correlation between grain orientation and the shade of color etching', *Mater Charact*, **61**, 814–817 (2010)
34. J. R. Davis, 'Metal Handbook Desk Edition' (1998)
35 R. M. Gorguluarslan, 'Multi-objective design optimization of additively manufactured lattice structures for improved energy absorption performance', *Proc Inst Mech Eng C J Mech Eng Sci*, **236**, 3–15 (2022)
36. W. D. Callister and D. G. Rethwisch, 'Materials Science and Engineering an Introduction' (2009)
37. W. B. Qurix, L. C. Edomwonyi-Otu, J. K. Aremu, G. J. Ibeh, S. G. Bawa, and D. Jise, 'The application of waste brass cartridges for gamma radiation shields and bullet proofing', *Journal of Materials Research and Technology*, **9** (2020)